Title

Miniaturized Wirelessly Powered and Controlled Implants for Multisite Stimulation.

Journal

IEEE Transactions on Microwave Theory and Techniques, 71(5)

ISSN

0018-9480

Authors

Habibagahi, Iman
Jang, Jaeeun
Babakhani, Aydin

Publication Date

2023-05-01

DOI

10.1109/tmtt.2022.3233368

Peer reviewed

HHS Public Access

Author manuscript

IEEE Trans Microw Theory Tech. Author manuscript; available in PMC 2024 May 01.

Published in final edited form as:

IEEE Trans Microw Theory Tech. 2023 May ; 71(5): 1911–1922. doi:10.1109/tmtt.2022.3233368.

Miniaturized Wirelessly Powered and Controlled Implants for Multisite Stimulation

Iman Habibagahi [Student Member, IEEE],
Jaeeun Jang [Member IEEE],
Aydin Babakhani [Member, IEEE]

Department of Electrical Engineering, University of California, Los Angeles, CA 90095 USA.

Abstract

This paper presents a miniaturized implant with a diameter of only 14 mm, which houses a novel System on Chip (SoC) enabling two voltage level stimulation of up to 16 implants using a single Tx coil. Each implant can operate at a distance of 80 mm in the air through the inductive resonant link. The SoC consumes only 27 μW static power and enables two channels with stimulation amplitudes of 1.8 V and 3.3 V and timing resolution of 100 μs. The SoC is implemented in the standard 180 nm complementary metal oxide semiconductor (CMOS) technology and has an area of 0.75 mm × 1.6 mm. The SoC comprises an RF rectifier, low drop-out regulator (LDO), error detection block, clock data recovery, finite state machine (FSM), and output stage. Each implant has a PCB-defined passcode, which enables the individual addressability of the implants for synchronized therapies. The implantable device weighs only 80 mg and sizes 20.1 mm^3. Tolerance of up to 70° to angular misalignment was measured at a distance of 50 mm. The efficacy of bilateral stimulation was further verified by implanting two devices on two sides of a pig's neck and performing bilateral vagus nerve stimulation (VNS), while monitoring the heart rate.

Keywords

biological effects and medical applications; data recovery; low power RFIC design; optimization; power transmission; RF system-on-chip (SOC) integration; CMOS RF design

I. Introduction

Multisite stimulation has proven helpful for different medical indications. In [1], the authors showed that specific stimulation patterns in the spinal cord could lead to unique muscle activation in mice. In [2], it was shown that multisite spinal cord stimulation enables faster recovery of motor functions. The efficacy of multisite stimulation has been proven for enhanced cardiac resynchronization therapy as well [3], [4], [5]. Both unilateral and bilateral VNS have proven to be useful for cardiac therapy [6], [7], epilepsy treatment [8], and weight control [9]. From the point of care perspective, miniaturized and battery-free implants are preferred since natural movements are maintained, and chances of infections or reoperation are minimized [10], [11], [12], [13].

Corresponding author: Iman Habibagahi, ihabibagahi@ucla.edu.

There have been multiple approaches to implementing multisite stimulation. As shown in Fig. 1(a), for spinal cord stimulation, authors have used electrode arrays to stimulate different nerves [10], [2], [1]. However, this approach is not easily scalable as the implant size and length of electrodes increase significantly with the number of stimulation sites. As presented in Fig. 1(b), in [3], the authors presented biventricular heart pacing with two implants operating with two carrier frequencies. The main drawback of this approach is that interference and unwanted couplings between Tx coils limit the operation distance. Furthermore, the number of Tx coils scales linearly with the number of implants, which shows the undesired scaling of the system. Fig. 1(c) presents a recent solution proposed in [14] to perform multisite stimulation. Physical unclonable function (PUF) IDs were implemented to address each implant individually. This approach benefits from good scalability; however, PUFs have inherent instability and sensitivity to process voltage and temperature variations (PVT) [15], [16]. Complex circuitry based on temporal majority voting (TMV) needs to be adopted to improve stability [17], [14], [15]. Furthermore, additional mask layers must be used in the fabrication process to implement Native NMOS transistors for PUFs which leads to higher fabrication costs [17], [14]. Double-tuned coil structures can also be used to control multiple implants in different frequency bands using a single Tx coil. However, their radiation efficiency is reduced, and the number of implants they can control is limited due to matching network complexity[18], [19].

To circumvent the abovementioned problems, we propose passcode-enabled miniaturized implants controlled by a single Tx coil, as shown in Fig. 1 (d). The 4-bit passcodes are defined on the chip's pads. Depending on the printed circuit board (PCB) connections, they are connected to VDD or VSS. This approach proposes a robust passcode for individual addressability. Tx coil powers all the implants simultaneously, and by using Pulse-width modulated amplitude-shift keying (PWM-ASK), implants are synchronized. Since each implant is deployed at a different site, there is no longer a need for long leads or electrode arrays. Furthermore, by optimizing link efficiency, a distance of 80 mm in air and 60 mm in phosphate-buffered saline (PBS) is achieved by using 2 W of peak power for the Tx coil. The proposed implant has the following features: (1) Reliable two-channel stimulation (1.8V or 3.3V); (2) Wirelessly powering and controlling up to 80 mm in air through an inductive 40.68 MHz link; (3) 4-bit passcode which enables up to 16 implants to operate at the same time; (4) Up to 70° angular misalignment can be tolerated; (5) Implants fabricated using standard FR4 substrate technology weigh only 80mg and have a volume of 20.1 mm^3; (6) Error detection block verifies if the implant has harvested enough power before stimulation. Fig. 2 shows a conceptual presentation of wirelessly powered and controlled implants for bilateral VNS with two implants.

This paper is an extended version of [20] with a detailed quantitative and qualitative discussion of the wireless power transfer (WPT) link co-design and circuit implementation. Additional experimental results for circuit validation and In-Vivo validation are provided. The rest of the paper is organized as follows: Section II describes coil design and wireless link parameters. Section III provides a detailed description of chip design, including rectifier, LDO, power-on reset (POR), clock data recovery (CDR), and output stage. Section IV presents measurement results, including circuit verification, *in vivo*, and *in vitro* validation. Section V concludes the paper.

II. Wireless link design

Magnetic resonance power transfer has been deployed in this work. Capacitive WPT is very sensitive to wireless link parameters [21], [22]. Ultrasound WPT relies on physical vibrations for power transfer. The main limitation of ultrasound is that it requires direct physical contact by applied gel and suffers from attenuation in muscle and bone mediums.

The main drawback of Magnetic resonance WPT is the large physical dimensions of the coil and tuning of the carrier frequency (f_c)[7], [23], [24]. The carrier frequency choice should be based on the application, safety, bandwidth, and minimum required distance [25], [26], [27]. In the next step, coil parameters can be optimized in a fixed distance and carrier frequency. Details of coil design are included in the following section. Furthermore, wireless link variations and rectifier non-linearity are investigated as pivotal factors for frequency tuning.

A. Coil Design

In this work, a matched series resonant Tx coil and parallel resonant Rx coil are chosen due to significantly lower power consumption on the implant side. This structure has superior efficiency in low-power applications [28]. Most of the design approaches involve an iterative process for coil design [23], [24], [29]. In our design, a similar approach for coil design is followed. The link efficiency is calculated from the equation below:

$$\eta_{link} \approx \frac{K^2 Q_{Tx} Q_L}{1 + K^2 Q_{Tx} Q_L} \times \frac{Q_L}{Q_L + Q_{Rx}} \tag{1}$$

In equation (1), K is the distance-dependent coupling factor, Q_{Tx} is the Tx coil quality factor ($Q_{Tx} = \omega L_{Tx}/R_{Tx}$), Q_{Rx} is the Rx coil quality factor ($Q_{Rx} = \omega L_{Rx}/R_{Rx}$), and Q_L is the loaded Rx coil quality factor which can be calculated from the following equation:

$$Q_L = \frac{1}{\frac{R_{Rx}}{\omega L_{Rx}} + \frac{\omega L_{Rx}}{R_L}} \tag{2}$$

In our design, a circular coil shape for Rx is chosen due to its higher quality factor [28]. The schematic of the inductively coupled coils is presented in Fig. 3(a). The quality (Q) and the coupling factor (K) can be calculated from the number of turns (N), spacing between turns (S), trace width (W), and distance between coil (d) [30]. The following steps are taken to design the Rx and Tx coil at a distance of 50 mm. For an initial design of the Tx coil, guidelines from [29], [31], [32] are taken into account, such as equal width and spacing ($W \approx S$), and the dimension of the optimal Tx coil (D) is less than the distance (d) from the following equation:

$$D \leq 2.288 \times d$$

(3)

Step1: Apply constraints on the Rx and Tx coil size.

Step2: Initialize N, W, S for Tx coil based on[29].

Step3: Optimize Rx coil parameters for best η_{link}.

Step4: Optimize Tx coil Parameters for best η_{link}.

Step5: Repeat until there is no improvement.

The simulated link efficiency in HFSS before matching is 2.17% at a distance of 50 mm with an unmatched coil and $R_L = 100k\Omega$. The physical dimensions of the simulated coils are shown in HFSS. Details of coil stand-alone parameters such as quality factor (Q), inductance (L), self-resonance-frequency (SRF), width (W), and spacing (S) of turns are presented in table I. The Tx coil is connected to the N5230C network analyzer directly for characterization. The Rx coil, due to its small size and high parasitics of the probes, is not measured directly, and HFSS simulation results are shown in the table I.

B. Wireless link Characterization

1) Biological Medium effects: Wireless link parameters such as power and medium variations can cause a change in the implant's resonant frequency[28], [31], [32]. The intervening biological medium can be approximated as the low-loss complex dielectric material. The real and imaginary part of the dielectric constant corresponds to electrical permittivity and conductivity, respectively. The equation below expresses the frequency-dependent dielectric constant:

$$\epsilon(f) = \epsilon_0\epsilon_1(f) + i\epsilon_2(f) = \epsilon'(f) + i\frac{\sigma(f)}{2\pi f} \tag{4}$$

In frequencies of a few MHz and above, the dielectric conductivity increase and permittivity decrease can no longer be ignored. The database of dielectric properties of different biological tissues is available at [33]. The dielectric properties are imported into HFSS to investigate the shift in resonance frequency after adding the material. Electrical permittivity and conductivity of skin, fat, and muscle are plotted in Fig. 4 (a) and (b), respectively. Depending on the application and animal size, the biological medium can vary. In our experiments, the implant is placed inside a pig's neck for VNS. The tissue is modeled with 3 mm of skin, 3 mm of fat, and 15mm of muscle on top of the implant, while the bottom of the implant is modeled as an infinite muscle due to the large size of the animal. Due to high electrical permittivity and conductivity, the effective capacitance of the coil increases, and the quality factor reduces after adding the biological tissue. The simulated implant inside the muscle and 3 MHz shift in resonance point is presented in Fig. 5 (a) and (b), respectively. It is possible to bring the resonance frequency back to 40.68 MHz by reducing C_p. Power transfer is done at 40.68 MHz to operate within the industrial, scientific, and medical (ISM)

band. The implant should work inside air and muscle properly. Therefore, the system's bandwidth (next section) should be high enough to cover the frequency shift.

2) Specific Absorption Rate: The specific absorption rate (SAR) is an essential figure of merit in determining how safe the wireless power transfer is to biological tissue. SAR can be calculated by the electric field inside the homogeneous tissue and can be calculated from the following equation:

$$SAR = \frac{\sigma \left| E_{rms}^2 \right|}{\rho} \tag{5}$$

σ is the electrical conductivity, and ρ is the density of the tissue. As stated earlier, conductivity increases with frequency, which results in a higher absorption rate. Federal Communication Commission (FCC) recognizes the limit of 1.6 W/kg for the human head. The simulated specific absorption rate is 2mW/kg in HFSS, which is three orders of magnitude less than the 10 W/kg safety limit according to IEEE Std C95.1–2005 and FCC regulation. The SAR is simulated over the human model with a port power of 1 W at 40.68 MHz when the Tx coil is placed 3 cm away. Fig. 6 shows simulated SAR in HFSS averaged on the human body. Based on the calculated SAR and link efficiency calculated link efficiency it is crucial to limit the average power consumption of the chip to hundreds of micro-watts to ensure safety.

III. Chip design

To ensure batteryless and wireless operation of the implantable device, a power harvesting chip should extract the passcode and control the stimulation. The chip is interfaced with the Rx coil to harvest the power and extract the clock and data. Tx sends data at the rate of 10 kbps with PWM-ASK modulation. Based on the pulse width, the clock and data can be extracted. Passcode detection is realized using a finite state machine (FSM) with received data, and stimuli voltage, amplitude, and duration are decided. At last, the output stage buffers the control signals and drives the tissue using standard cuff-electrodes. On-chip error detection block ensures that the harvested voltage is not lower than 2.6 V during stimulations. The overall view of the implant block diagram is presented in Fig. 7.

A. Power management unit

Power management is crucial for the implantable device to operate reliably. The rectifier harvests power from the Rx coil and stores them on an off-chip capacitor (C_{Str}). The LDO and reference generation are also essential for reliable and efficient operation. Each block is discussed in detail in the following sections.

1) Rectifier: Passive rectifiers have the advantage of efficient cold start-up [34], [35], [36]. Cross-coupled (CC) full-wave rectifier topology has been chosen due to its excellent power transfer efficiency and dynamic threshold voltage (V_{th}) compensation [34]. The proposed rectifier is shown in Fig. 8 (a). The limiter sets the maximum harvested voltage

to be 3.8 V, and LDO provides a stable 1.8 V when the rectifier voltage reaches 1.8 V. A single stage of the CC rectifier is shown in Fig. 8 (b). The current in the positive cycle flows through M_{p1} and M_{n2}, and during the negative cycle, they flow through M_{p2} and M_{n1}. The NMOS and PMOS are scaled with a constant ratio according to their mobility. The compensation capacitor is set to 0.5 pF to compensate for the mismatches between the transistors [34]. The coupling capacitor enables dynamic gate biasing of the CC rectifier needs to be large enough ($C_c = 6$ pF) so that no voltage drop across the capacitor. One of the challenging parts of the rectifier design is choosing the number of stages and sizing of the transistors. The higher number of stages and transistor widths leads to higher bandwidth (BW) while the sensitivity of the rectifier is reduced [37], [32]. As shown in Fig. 8, the rectifier impedance can be presented with parallel resistance (R_{in}) and capacitance (C_{in}).

The quality factor can be expressed based on (2), and for a properly designed Rx coil, the power going to the rectifier is much larger than the power wasted in the coil, therefore:

$$Q_{Rect} < < Q_{Rx} = \frac{L_{Rx}\omega}{R_{Rx}} \tag{6}$$

$$Q_L \approx Q_{Rect} = \frac{R_{in}}{L_{Rx}\omega} \tag{7}$$

And therefore, its bandwidth can be calculated from the following equation:

$$BW = \frac{f_0}{Q_{Rect}} \tag{8}$$

The inherent efficiency of the rectifier is another important parameter which is defined as:

$$\eta_{Rect} = \frac{P_{DC}}{P_{RF}} \tag{9}$$

According to [32], the sensitivity of the rectifier can be calculated as $Q\eta_{Rect}$.

The simulated results of rectifier BW and $Q\eta_{Rect}$ when the rectifier is loaded by 10 μA of current are shown in Fig. 9 (a) and (b), respectively. It should be noted that while scaling the width of the transistors, the constant ratio is preserved. In this work, four stages of the CC rectifier with W/L= $4\mu m/180nm$ are chosen for the NMOS transistors. This choice results in BW of 5.377 MHz and $Q\eta_{Rect}$ of 0.486.

The resonance frequency of the Rx coil can be calculated using the equation below:

$$f_{Res} = \frac{1}{2\pi\sqrt{(C_{in} + C_{tune})L_{Rx}}} \quad (10)$$

The rectifier is a non-linear block, and its input impedance varies with power and loading[38]. As shown in Fig. 10 (a) and (b), the input resistance varies with load and input power, but more importantly, input capacitance (C_{in}) varies considerably with input power. Variation of input power for a wirelessly powered implant is inevitable, leading to the variation of the resonance frequency (f_{Res}) based on (10). Fig. 10 (c) shows the 1.6 MHz shift in f_{Res} due to non-linear input capacitance.

In [39], the authors propose a complex mechanism to adaptively change the tuning capacitor to maintain a constant resonant frequency. In this work, BW is chosen wide enough, so resonance resistance does not drop more than 15% of its nominal value.

The procedure of co-designing the Rx coil and rectifier is shown in Fig. 11. Unlike [32], in this work, the Tx frequency is constant, and the goal is to design an Rx coil and rectifier such as it can work at different mediums and power levels. The initial design of the Rx coil is discussed in the previous section. It has to be verified that the coil satisfies (6). In the next step, a reasonable value for the rectifier's efficiency (50%) and BW (3 MHz) is chosen. In the third step, possible variations, including adding biological tissue (discussed in the previous section) and rectifier non-linearity, are simulated. Lastly, it is verified that the rectifier can tolerate these variations without losing more than 50 % of its performance. The Rx coil must be redesigned for a higher BW if the variations cannot be tolerated. The high available BW at the same Q is the advantage of choosing 40.68 MHz compared to the lower frequency bands (ex: 13.56 MHz). However, it is more challenging to satisfy SAR regulations due to higher tissue absorption, as shown in Fig. 4.

2) LDO: Low drop-out regulator is essential to the chip as it provide a stable 1.8 supply for other blocks. The schematic of LDO is shown in Fig. 12. V_{ref1} and V_{ref2} are set to 2.64 V and 0.33 V, respectively; the architecture of the reference generator is the same as the one presented in the [31]. The two-stage LDO consists of an error amplifier and the pass transistor as a controlled current source. This structure benefits from higher loop gain, and a lower voltage drop-out than the source follower pass transistor [40], [41]. The main drawback of this structure is the low phase margin which can cause ringing issues. The trade-off between BW and phase margin is established depending on the LDO output capacitance. Miller compensation capacitance (C_c) of 3 pF has been added to improve the phase margin. The proposed LDO has a loop gain of 34.1 dB and a phase margin of 89.94 at 62.3 Hz while loaded with a 1 μF off-chip capacitor. The most important features of the LDO are summarized in table II. The quiescent power consumption of the LDO (I_Q) is the amount of current the LDO takes at no-load conditions. Line regulation is another important figure of merit for LDO, defined as:

$$LineRegulation = \frac{\Delta V_{LDO}}{\Delta V_{Rect}} \times 100\% \tag{11}$$

Line regulation identifies the ratio between regulated voltage and supply voltage variations. Load Regulation is also defined as the amount of the LDO voltage drop concerning a change in the loading current [40]. The output resistance of the LDO is also tightly related to the load regulation in a small signal domain by the following equation:

$$R_{on} = \frac{\delta V_{LDO}}{\delta I_{load}} \tag{12}$$

3) POR: It is crucial for a wirelessly powered device to reset the digital blocks every time the chip is powered up. The cross-coupled inverter chain similar to [42] is used for POR. A fraction of rectifier voltage ($\alpha = 0.75$) is used for a weak current source to charge the capacitor in cross-coupled inverters. The inverters are sized for opposite pull-up and pull-down to prevent metastability. As shown in Fig. 13, the generated pulse is further extended by capacitively loaded inverter chain to 50 ns. The digital blocks are reset every time the harvested voltage reaches 0.9 V.

B. Clock and data recovery

Clock and data recovery are essential to determine the stimulation's passcode, duration, and voltage level. Unlike power-hungry phase detectors [43], the difference between the pulse width of bit '1' and '0' can be utilized to recover the clock and data [44], [45]. In this work, bits '1' and '0' have pulse widths of 75% and 25% respectively, and the duration of each bit is set to be 100 μs. The signal's envelope can be used as the clock for the system. Fig. 14 shows that one stage of the cross-coupled rectifier can operate as a self-mixer [43]. The signal at the antenna side (V_{ANT}) is passed through a self-mixer (V_1) and low pass filtered (V_2) with a corner frequency of 2.1 kHz. The 10 pF capacitor at the output of the mixer is to filter out the $2f_{RF}$ frequency. The comparator is needed in the next stage to remove the DC components [46]. Self-mixing action can be expressed using the equations below:

$$V_{ANT} = A[1 - mx(t)]cos(2\pi f_{RF}t) \tag{13}$$

$$V_1 \approx A[1 - mx(t)]cos(2\pi f_{RF}t) \times \frac{2}{\pi}cos(2\pi f_{RF}t) \tag{14}$$

$$V_{1,LPF} = \frac{A}{\pi}[1 - mx(t)]$$

(15)

In Fig. 14, the simulation for OOK ($m = 100\%$) is presented. However, to save power and maintain a good power transfer efficiency (PTE) during data transfer, the modulation index (m) can reduce to 5%. To increase stability and noise robustness, a Schmitt trigger is added [46]. The circuit schematic of the comparator and Schmitt trigger are presented in Fig. 15. The comparator has a gain of 51 dB with 4 MHz bandwidth, and the Schmitt trigger has a hysteresis window of 0.35 V to 0.95 V. The reference generator introduced in [47] is used due to fast start-up and temperature stability.

Monte Carlo over 204 post-layout simulations is performed. As shown in Fig. 16, The standard deviation (σ) of the recovered signal frequency is 0.154 Hz which shows accurate clock recovery with process variations.

The clock is integrated by a 40 nA current source on a 1.8 pF capacitor. Bit '1' and '0' reach values of 1.65 V and 0.375 V after integration (V_{int}). After comparing with the reference voltage of 1.25 V, a pulse of 18 μs is generated if the bit is '1'. In order to avoid glitches, a delay of 6 μs is applied for the detected pulses; then they are passed through a shift register to generate the data (D_0) for passcode detection and stimulation.

Each chip has a specific 4-bit passcode based on the PCB connections. After sending 8 bits, including flag and voltage level, if the passcode and flag are matched, the stimulation activates. Fig. 17 (a) shows the timing diagram of the proposed chip and how independent channels stimulate. Fig. 17 (b) shows the FSM for stimulation. The error signal generated for the output stage verifies if enough voltage is harvested on the storage capacitor. Stimulation happens only when the error signal is zero.

C. Output stage

Fig. 18 shows the output stage of the stimulator. An error detection block will stop the stimulation if the harvested voltage drops below 2.6 V. A conventional differential cascode voltage switch (DCVS) is chosen due to its low static power consumption and fast switching [48]. DCVS shifts the control signal from 1.8 V to 3.3 V domain. NMOS transistors are scaled up to ensure a strong pull-down network. The signal after buffering has a 1 ns delay. The static and dynamic power (f=10 KHz) consumption of the output stage with buffers is 30 pW and 155 nW, respectively.

The minimum tolerable load resistance for the storage capacitor can be defined as:

$$R_{load,\,min} = \frac{V_{Stim,\,Avg} \times t_{Stim}}{C_{str} \times \Delta V_{stim}}$$

(20)

Where $V_{Stim,\,Avg}$ is the average stimulation voltage, t_{Stim} is the stimulation pulse time, C_{str} is the storage capacitance, and ΔV_{stim} is the maximum allowable voltage change during stimulation. For a conventional stimulation of $t_{Stim} = 1$ ms, $V_{Stim,\,Avg} = 3.3$ V and $\Delta V_{stim} = 0.3$ V, the $R_{load,\,min}$

is 271Ω. The maximum load for stable stimulation must be verified to be within operating range.

IV. Measurement results

A. Chips measurments

The proposed SoC is fabricated in TSMC 180-nm technology. The chip has an area of $1.2mm^2$, as shown in Fig. 19. The performance of the Rectifier and LDO in a stand-alone setup is measured. Fig. 20 (a) shows the harvested voltage (V_{Rect}) and regulated voltage (V_{LDO}) when the RF voltage source is driving the chip. As expected, the harvested voltage is limited to 3.8 V, and the output of LDO stays at 1.8 V. The total simulated power consumption of the chip is $27\mu W$, where LDO takes the largest portion of the power consumption (See Fig. 20 (b)). In the next measurement, demodulated passcode was observed while changing the carrier frequency (f_c) and modulation index (m). As presented in Fig. 21, the chip can work at frequencies up to 1080 MHz. However, the optimum results are achieved when a carrier frequency of 40.68 MHz is chosen. This choice allows the modulation index to reduce as low as 10% to have a negligible power drop during data transfer.

B. Implant measurements

The chip, storage capacitors, and cuff electrodes are assembled on the miniaturized circular PCB. Additional filtering capacitors ($C_{filt} = 10\mu F$) are added in series for charge balancing[7], [3]. Due to the small form factor of the implant coil, its inductance cannot be measured accurately by a network analyzer. Therefore, for the frequency tuning, a wideband unmatched transmitter coil can be used to power the implant, and harvested voltage is measured at different frequencies[7]. A tuning capacitor is tuned in steps of 0.1 pF, and the optimized value of 8 pF yields the harvested voltage of 3.5 V. The end-to-end efficiency is calculated using the equation below:

$$PTE = \frac{P_{chip} + P_{stim} \times D_{stim}}{P_{Tx} \times D_{Tx}} \times 100\% \quad (17)$$

Where P_{chip}, P_{stim} and P_{Tx} are chip power consumption, stimulation power, and transmitted power and D_{stim} and D_{Tx} are duty cycles for stimulation and transmitters. In this equation, since stimulation is only on $100\mu s$ every 1s ($D_{stim} = 0.01\%$), the stimulation term can be neglected from the equation. The transmitter is tuned on for 5ms every 1s ($D_{Tx} = 0.5\%$) with $P_{Tx} = 2W$. The overall calculated efficiency for this distance of 50 mm is 0.27%.

As presented in Fig. 22 (a) and (b), the implant's cuff electrodes are connected to an oscilloscope for monitoring. RF signal generator (E4428C, Hewlett Packard Inc.) is connected to a power amplifier (ZHL-20 W-13 +, Mini-Circuits Inc.) to generate a peak power of 2 W. An arbitrary waveform generator (AWG-Agilent 33522A) modulates the RF generator for power and data transmission. The implant is loaded with 1kΩ and $1\mu F$ capacitor to mimic tissue impedance [3]. The sphere-shaped receiver coils offer more resilience to misalignments [49]. However, in this work, we have used a planar coil to reduce

volume and improve ease of fabrication and assembly. Fig. 23 (a) shows the harvested voltage vs. distance. The minimum harvested voltage for the implant before the error signal activation is 2.6 V. Two protractors for Tx and Rx coils are installed to measure misalignment. Fig. 23 (b) shows angular misalignment tolerance of up to 70° at a distance of 50 mm. Due to the symmetrical nature of the coils, there is no sensitivity for Z-axis misalignment, and there is similar sensitivity for X and Y-axis misalignment (axis shown in Fig. 22 (a)). At a vertical distance of 50 mm, the maximum allowable lateral misalignment before the voltage reaches 2.6 V is 30 mm.

In another setup, different passcodes are sent to different implants with passcodes. It was observed the stimulation only happens when transmitted passcodes match with the PCB-defined passcodes. Examples of both 3.3 V and 1.8 V stimulation are shown in Fig. 24 while the oscilloscope loaded the implant.

C. In-Vivo validation

The implants were encapsulated with biocompatible epoxy (EPO-TEK MED-301-2FL) for isolation and portability. Two implants are put inside the anesthetized Yorkshire pig's left and right side of the neck for bilateral VNS. In the first step using a PalmSens4 Electrochemical Impedance Spectroscopy (EIS) device [7], the impedance across cuff electrodes is measured to verify that they satisfy minimum load conditions as introduced in (16). The EIS measures the tissue's frequency response (1 Hz −10 kHz, $V_{AC} = 10$ mV) and records its magnitude and phase. The results are presented in Fig. 25. The fitted circuits using the PalmSense circuit fitting tool are shown on the bottom left of each picture. As shown in Fig. 25, the worst case impedance for the right and left vagus nerve is 1.81 $k\Omega$ and 2.55 $k\Omega$, respectively. These impedances satisfy the minimum resistance requirement introduced in (16) for HV (3.3 V) stimulation.

The In-Vivo validation is performed by delivering two different passcodes to the left and right implants using a single Tx coil, as shown in Fig. 26 (a) and (b). The stimulation duration was set to 10 s, the voltage set to 3.3 V, and the pulse duration was set to 1 ms, similar to [6], [7]. Cardiac control, based on the principle of the optimized VNS, can be elicited from either of the vagus nerves [6], [50]. In this work, the RF signal generator was connected to the power amplifier to provide a stable power of 2 W at 40.68 MHz. The modulation is done using an external AWG. Tx coil is placed 54 mm above the implants (including 10mm implantation depth), and different passcodes are transmitted for unilateral (right side only) and bilateral (both sides) VNS. The pig's heart rate (HR) was monitored using standard electrocardiogram (EKG) electrodes. Fig. 26 shows conceptual and actual pictures of *in-vivo* setup. It was observed that the drop in HR was proportional to stimulation frequency and bilateral stimulation induced a stronger response. Fig. 27 shows HR change for bilateral and unilateral stimulation. HR drop concerning baseline for unilateral VNS was 24.4% and 12.6% at 10 Hz and 20 Hz, respectively. For bilateral 10 Hz stimulation, HR drop was measured to be 22.5%, which is similar to unilateral stimulation with double the frequency. The results indicate successful passcode detection and efficacy of bilateral VNS.

D. Performance summary

The performance of the proposed implant is compared to the state-of-the-art wireless implant introduced in [14], [3], [51], [11], [10]. The proposed implants in [14], operate based on PUF, which needs additional native layers for fabrication, and complex circuitry is needed to ensure PVT stability. In this work, only two bits are used as the preamble. However, a larger number of preamble bits can improve the security of the device. The implants proposed in [3] can operate independently without data transfer. However, the main drawback is the higher number of Tx coils and interference between coils. Similarly, approaches in [51], [10] suffer from scalability issues. Magneto-electric (ME) and ultrasonic [17], [14], [11] power transfer still need to show their performance in big animals. Compared to commercial VNS therapy implants [52], our proposed implant is about 1000 times smaller in size, and batteryless operation improves safety. The device weighs only 80 mg without cuff electrodes and has two channel constant voltage capability similar to state-of-the-art technologies.

V. Conclusion

The proposed implantable system enables WPT and synchronized control of up to 16 sites using a single Tx coil. The proposed SoC, implemented in 180 nm technology, consumes only 27 μW of static power, and simulated SAR is 3 orders of magnitude lower than the safety limit (IEEE Std C95.1-2005). The Rx coil resonant frequency can vary based on the presence of biological tissue and Tx power level. An optimization algorithm for co-designing the rectifier and Rx coil is proposed in the paper to ensure that the implant can work reliably in different mediums and power levels. Each implant can deliver 1.8 V or 3.3 V pulses with 100 μs accuracy. A criterion for maximum loading of the implants is defined, and tissue impedances are verified to be within the range. Angular misalignment of up to 70° is tolerable at a distance of 50 mm. Bilateral and unilateral VNS is verified in pigs at a distance of 54 mm. The features mentioned above bring the potential for future clinical applications. The optimization algorithms can also be used as a platform for future wirelessly powered devices.

Acknowledgments

The authors would like to thank Prof. Jeffrey Ardell and Dr. Joseph Hadaya for providing helpful discussions and supporting *in-vivo* testing. The National Institute of Health partially supported the research reported in this paper. We thank Arkaprova Ray, Roshan P. Mathews, and Hamid Sharemi for their valuable comments and discussion.

This work was partially supported by the National Institute of Health (NIH).

Animal studies were approved by the University of California, Los Angeles Institutional Animal Care and Use Committee (IACUC). At the end of the study, animals were euthanized in accordance with the approved IACUC protocol and the National Institutes of Health's Guide for the Care and Use of Laboratory Animals. All methods reported are in accordance with Animal Research: Reporting of In Vivo Experiments (ARRIVE) guidelines.

Biographies

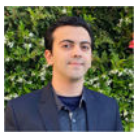

Iman Habibagahi Iman Habibagahi (Graduate Student Member, IEEE) received a B.Sc. degree in electrical engineering from the Sharif University of Technology, Tehran, Iran, in 2019, and an M.Sc. degree from the University of California Los Angeles (UCLA), Los Angeles, CA, USA, in 2021. He is currently pursuing a Ph.D. degree at the University of California at Los Angeles, Los Angeles, CA, USA, advised by Prof. A. Babakhani. His research interests include low-power integrated circuit design, wireless power harvesting, and wireless technologies for biomedical implants. Mr. Habibagahi received the UCLA ECE department Fellowship and RFIC'22 NSF student travel award.

Jaeeun Jang Jaeeun Jang (S'13-M'19) received B.S., M.S., and Ph.D. in electrical engineering from the Korea Advanced Institute of Science and Technology (KAIST), Daejeon, Korea, in 2014, 2016, and 2019, respectively. In 2020, he joined the University of California, Los Angeles, CA, USA as a postdoctoral researcher. Since 2022, he has been with Samsung Electronics, Hwaseong, S. Korea as a staff engineer. He has worked on developing a low-power wireless transceiver and wearable, implantable healthcare system. His research interests include the design of ultra-low-power analog/mixed-mode, wireless power transfer, healthcare/medical sensor systems, and the RFIC design.

Aydin Babakhani Dr. Babakhani is an Associate Professor in the Electrical and Computer Engineering Department at UCLA and the Director of UCLA Integrated Sensors Laboratory. Prior to joining UCLA, he was an Associate Professor in the Electrical and Computer Engineering Department at Rice University and the Director of Rice Integrated Systems and Circuits Laboratory. He was a Louis Owen Junior Chair Assistant Professor (2016–2017) and Assistant Professor of ECE (2011–2016) at Rice University. He was a member of the DARPA Microsystems Exploratory Council (MEC) from 2017 to 2021. He is a co-founder of Maxwell Biomedical Inc., MicroSilicon Inc., and Nervonik Inc. He received his B.S. degree in electrical engineering from the Sharif University of Technology in 2003 and his M.S. and Ph.D. degrees in Electrical Engineering from Caltech in 2005 and 2008,

respectively. He was a postdoctoral scholar at Caltech in 2009 and a research scientist at IBM Thomas J. Watson Research Center in 2010.

Dr. Babakhani has been awarded multiple best paper awards, including the Best Paper Award at the IEEE SiRF conference in 2016, the Best Paper Award at the IEEE RWS Symposium in 2015, the Best Paper Award at the IEEE IMS Symposium in 2014, and the 2nd-place in the Best Paper Awards at the IEEE APS Symposium 2016 and IEEE IMS Symposium 2016. He was a plenary speaker at the International Instrumentation and Measurement Technology Conference in 2018 and a plenary speaker at the International Conference on Infrared, Millimeter, and Terahertz waves (IRMMW-THz) in 2017. He has published more than 120 papers in peer-reviewed journals and conference proceedings as well as 30 issued or pending patents. His research is supported by NSF, NIH, DOE, DARPA, AFOSR, ONR, the W. M. Keck Foundation, SRC, and more than 10 companies. He won a Nokia Bell Labs Prize in 2018, a prestigious NSF CAREER award in 2015, an Innovation Award from Northrop Grumman in 2014, and a DARPA Young Faculty Award in 2012. He also received the Caltech Electrical Engineering Department's Charles Wilts Best Ph.D. Thesis Prize for his work titled "Near-Field Direct Antenna Modulation." He was the recipient of the Microwave Graduate Fellowship in 2007, the Grand Prize in the Stanford-Berkeley-Caltech Innovators Challenge in 2006, the Analog Devices Inc. Outstanding Student Designer Award in 2005, as well as a Caltech Special Institute Fellowship, and an Atwood Fellowship in 2003. He was also the Gold Medal winner at both the National Physics Competition in 1998 and the 30th International Physics Olympiad in Padova, Italy, in 1999.

References

[1]. Hogan MK, Barber SM, Rao Z, Kondiles BR, Huang M, Steele WJ, Yu C, and Horner PJ, "A wireless spinal stimulation system for ventral activation of the rat cervical spinal cord," Scientific Reports, vol. 11, no. 1, pp. 1–16, 2021. [PubMed: 33414495]

[2]. Gerasimenko Y, Gorodnichev R, Puhov A, Moshonkina T, Savochin A, Selionov V, Roy RR, Lu DC, and Edgerton VR, "Initiation and modulation of locomotor circuitry output with multisite transcutaneous electrical stimulation of the spinal cord in noninjured humans," Journal of neurophysiology, vol. 113, no. 3, pp. 834–842, 2015. [PubMed: 25376784]

[3]. Lyu H, John M, Burkland D, Greet B, Post A, Babakhani A, and Razavi M, "Synchronized biventricular heart pacing in a closed-chest porcine model based on wirelessly powered leadless pacemakers," Scientific reports, vol. 10, no. 1, pp. 1–9, 2020. [PubMed: 31913322]

[4]. Gutruf P, Yin RT, Lee KB, Ausra J, Brennan JA, Qiao Y, Xie Z, Peralta R, Talarico O, Murillo A. et al. , "Wireless, battery-free, fully implantable multimodal and multisite pacemakers for applications in small animal models," Nature communications, vol. 10, no. 1, pp. 1–10, 2019.

[5]. Leon AR, Greenberg JM, Kanuru N, Baker CM, Mera FV, Smith AL, Langberg JJ, and DeLurgio DB, "Cardiac resynchronization in patients with congestive heart failure and chronic atrial fibrillation: effect of upgrading to biventricular pacing after chronic right ventricular pacing," Journal of the American College of Cardiology, vol. 39, no. 8, pp. 1258–1263, 2002. [PubMed: 11955841]

[6]. Ardell JL, Rajendran PS, Nier HA, KenKnight BH, and Armour JA, "Central-peripheral neural network interactions evoked by vagus nerve stimulation: functional consequences on control of cardiac function," American Journal of Physiology-Heart and Circulatory Physiology, vol. 309, no. 10, pp. H1740–H1752, 2015. [PubMed: 26371171]

[7]. Habibagahi I, Omidbeigi M, Hadaya J, Lyu H, Jang J, Ardell JL, Bari AA, and Babakhani A, "Vagus nerve stimulation using a miniaturized wirelessly powered stimulator in pigs," Scientific reports, vol. 12, no. 1, pp. 1–12, 2022. [PubMed: 34992227]

[8]. Nune G, DeGiorgio C, and Heck C, "Neuromodulation in the treatment of epilepsy," Current treatment options in neurology, vol. 17, no. 10, pp. 1–6, 2015.

[9]. Yao G, Kang L, Li J, Long Y, Wei H, Ferreira CA, Jeffery JJ, Lin Y, Cai W, and Wang X, "Effective weight control via an implanted self-powered vagus nerve stimulation device," Nature communications, vol. 9, no. 1, pp. 1–10, 2018.

[10]. Lee B, Koripalli MK, Jia Y, Acosta J, Sendi M, Choi Y, and Ghovanloo M, "An implantable peripheral nerve recording and stimulation system for experiments on freely moving animal subjects," Scientific reports, vol. 8, no. 1, pp. 1–12, 2018. [PubMed: 29311619]

[11]. Piech DK, Johnson BC, Shen K, Ghanbari MM, Li KY, Neely RM, Kay JE, Carmena JM, Maharbiz MM, and Muller R, "A wireless millimetre-scale implantable neural stimulator with ultrasonically powered bidirectional communication," Nature Biomedical Engineering, vol. 4, no. 2, pp. 207–222, 2020.

[12]. Burton A, Won SM, Sohrabi AK, Stuart T, Amirhossein A, Kim JU, Park Y, Gabros A, Rogers JA, Vitale F. et al. , "Wireless, battery-free, and fully implantable electrical neurostimulation in freely moving rodents," Microsystems & nanoengineering, vol. 7, no. 1, pp. 1–12, 2021. [PubMed: 34567721]

[13]. Jang J, Habibagahi I, Rahmani H, and Babakhani A, "Wirelessly powered, batteryless closed-loop biopotential recording ic for implantable leadless cardiac monitoring applications," in 2021 IEEE Biomedical Circuits and Systems Conference (BioCAS). IEEE, 2021, pp. 1–4.

[14]. Yu Z, Chen JC, He Y, Alrashdan FT, Avants BW, Singer A, Robinson JT, and Yang K, "Magnetoelectric bio-implants powered and programmed by a single transmitter for coordinated multisite stimulation," IEEE Journal of Solid-State Circuits, vol. 57, no. 3, pp. 818–830, 2021. [PubMed: 36275505]

[15]. Li D. and Yang K, "A self-regulated and reconfigurable cmos physically unclonable function featuring zero-overhead stabilization," IEEE Journal of Solid-State Circuits, vol. 55, no. 1, pp. 98–107, 2019.

[16]. Mathew SK, Satpathy SK, Anders MA, Kaul H, Hsu SK, Agarwal A, Chen GK, Parker RJ, Krishnamurthy RK, and De V, "16.2 a 0.19 pj/b pvt-variation-tolerant hybrid physically unclonable function circuit for 100% stable secure key generation in 22nm cmos," in 2014 IEEE International Solid-State Circuits Conference Digest of Technical Papers (ISSCC). IEEE, 2014, pp. 278–279.

[17]. Yu Z, Chen JC, He Y, Alrashdan FT, Avants BW, Singer A, Robinson JT, and Yang K, "Multisite bio-stimulating implants magnetoelectrically powered and individually programmed by a single transmitter," in 2021 IEEE Custom Integrated Circuits Conference (CICC). IEEE, 2021, pp. 1–2.

[18]. Habibagahi I, Mathews RP, Ray A, and Babakhani A, "Design and implementation of multisite stimulation system using a double-tuned transmitter coil and miniaturized implants," IEEE Microwave and Wireless Components Letters, 2022.

[19]. Kung M-L and Lin K-H, "Enhanced analysis and design method of dual-band coil module for near-field wireless power transfer systems," IEEE Transactions on Microwave Theory and Techniques, vol. 63, no. 3, pp. 821–832, 2015.

[20]. Habibagahi I, Jang J, and Babakhani A, "Miniaturized wirelessly powered and controlled implants for vagus nerve stimulation," in 2022 IEEE Radio Frequency Integrated Circuits Symposium (RFIC). IEEE, 2022.

[21]. Erfani R, Marefat F, and Mohseni P, "Biosafety considerations of a capacitive link for wireless power transfer to biomedical implants," in 2018 IEEE Biomedical Circuits and Systems Conference (BioCAS). IEEE, 2018, pp. 1–4.

[22]. Jegadeesan R, Agarwal K, Guo Y-X, Yen S-C, and Thakor NV, "Wireless power delivery to flexible subcutaneous implants using capacitive coupling," IEEE Transactions on Microwave Theory and Techniques, vol. 65, no. 1, pp. 280–292, 2016.

[23]. Cheng Y, Wang G, and Ghovanloo M, “Analytical modeling and optimization of small solenoid coils for millimeter-sized biomedical implants,” IEEE Transactions on Microwave Theory and Techniques, vol. 65, no. 3, pp. 1024–1035, 2016.

[24]. Jow U-M and Ghovanloo M, “Design and optimization of printed spiral coils for efficient transcutaneous inductive power transmission,” IEEE Transactions on biomedical circuits and systems, vol. 1, no. 3, pp. 193–202, 2007. [PubMed: 23852413]

[25]. Poon AS, O’Driscoll S, and Meng TH, “Optimal frequency for wireless power transmission into dispersive tissue,” IEEE Transactions on Antennas and Propagation, vol. 58, no. 5, pp. 1739–1750, 2010.

[26]. Kim S, Ho JS, and Poon AS, “Wireless power transfer to miniature implants: Transmitter optimization,” IEEE Transactions on Antennas and Propagation, vol. 60, no. 10, pp. 4838–4845, 2012.

[27]. Kim S, Ho JS, and Poon AS, “Midfield wireless powering of subwavelength autonomous devices,” Physical review letters, vol. 110, no. 20, p. 203905, 2013. [PubMed: 25167413]

[28]. Pérez-Nicoli P, Silveira F, and Ghovanloo M, Inductive Links for Wireless Power Transfer. Springer, 2021.

[29]. Zargham M. and Gulak PG, “Maximum achievable efficiency in near-field coupled power-transfer systems,” IEEE Transactions on Biomedical Circuits and Systems, vol. 6, no. 3, pp. 228–245, 2012. [PubMed: 23853145]

[30]. Ahn D. and Ghovanloo M, “Optimal design of wireless power transmission links for millimeter-sized biomedical implants,” IEEE transactions on biomedical circuits and systems, vol. 10, no. 1, pp. 125–137, 2015. [PubMed: 25616074]

[31]. Rahmani H. and Babakhani A, “A dual-mode rf power harvesting system with an on-chip coil in 180-nm soi cmos for millimeter-sized biomedical implants,” IEEE Transactions on Microwave Theory and Techniques, vol. 67, no. 1, pp. 414–428, 2018.

[32]. Lyu H, Gad P, Zhong H, Edgerton VR, and Babakhani A, “A 430-mhz wirelessly powered implantable pulse generator with intensity/rate control and sub-1 μa quiescent current consumption,” IEEE transactions on biomedical circuits and systems, vol. 13, no. 1, pp. 180–190, 2018. [PubMed: 30418917]

[33]. Hasgall P, Di Gennaro F, Baumgartner C, Neufeld E, Lloyd B, Gosselin M, Payne D, Klingenböck A, and Kuster N, “It-is database for thermal and electromagnetic parameters of biological tissues, 2018. itis. swiss/database. doi: 10.13099/VIP21000-04-0, Tech. Rep.

[34]. Kotani K, Sasaki A, and Ito T, “High-efficiency differential-drive cmos rectifier for uhf rfids,” IEEE Journal of Solid-State Circuits, vol. 44, no. 11, pp. 3011–3018, 2009.

[35]. Papotto G, Carrara F, and Palmisano G, “A 90-nm cmos threshold-compensated rf energy harvester,” IEEE Journal of solid-state circuits, vol. 46, no. 9, pp. 1985–1997, 2011.

[36]. Li X, Mao F, Lu Y, and Martins RP, “A vhf wide-input range cmos passive rectifier with active bias tuning,” IEEE Journal of Solid-State Circuits, vol. 55, no. 10, pp. 2629–2638, 2020.

[37]. Lyu H, Liu X, Sun Y, Jian Z, and Babakhani A, “A 915-mhz far-field energy harvester with- 22-dbm sensitivity and 3-v output voltage based on antenna-and-rectifier codesign,” IEEE Microwave and Wireless Components Letters, vol. 29, no. 8, pp. 557–559, 2019.

[38]. Stoopman M, Keyrouz S, Visser HJ, Philips K, and Serdijn WA, “Co-design of a cmos rectifier and small loop antenna for highly sensitive rf energy harvesters,” IEEE Journal of Solid-State Circuits, vol. 49, no. 3, pp. 622–634, 2014.

[39]. Lyu H. and Babakhani A, “A 13.56-mhz- 25-dbm-sensitivity inductive power receiver system-on-a-chip with a self-adaptive successive approximation resonance compensation front-end for ultra-low-power medical implants,” IEEE Transactions on Biomedical Circuits and Systems, vol. 15, no. 1, pp. 80–90, 2020.

[40]. Rincon-Mora GA and Allen PE, “A low-voltage, low quiescent current, low drop-out regulator,” IEEE journal of Solid-State circuits, vol. 33, no. 1, pp. 36–44, 1998.

[41]. Razavi B, “The low dropout regulator [a circuit for all seasons],” IEEE Solid-State Circuits Magazine, vol. 11, no. 2, pp. 8–13, 2019.

[42]. Pivonka D, Yakovlev A, Poon AS, and Meng T, “A mm-sized wirelessly powered and remotely controlled locomotive implant,” IEEE transactions on biomedical circuits and systems, vol. 6, no. 6, pp. 523–532, 2012. [PubMed: 23853253]

[43]. Rajavi Y, Taghivand M, Aggarwal K, Ma A, and Poon AS, “An rf-powered fdd radio for neural microimplants,” IEEE Journal of Solid-State Circuits, vol. 52, no. 5, pp. 1221–1229, 2017.

[44]. Charthad J, Weber MJ, Chang TC, and Arbabian A, “A mm-sized implantable medical device (imd) with ultrasonic power transfer and a hybrid bi-directional data link,” IEEE Journal of solid-state circuits, vol. 50, no. 8, pp. 1741–1753, 2015.

[45]. Charthad J, Chang TC, Liu Z, Sawaby A, Weber MJ, Baker S, Gore F, Felt SA, and Arbabian A, “A mm-sized wireless implantable device for electrical stimulation of peripheral nerves,” IEEE transactions on biomedical circuits and systems, vol. 12, no. 2, pp. 257–270, 2018. [PubMed: 29578414]

[46]. Rahmani H. and Babakhani A, “A wirelessly powered reconfigurable fdd radio with on-chip antennas for multi-site neural interfaces,” IEEE Journal of Solid-State Circuits, vol. 56, no. 10, pp. 3177–3190, 2021.

[47]. Gunawan M, Meijer GC, Fonderie J, and Huijsing JH, “A curvature-corrected low-voltage bandgap reference,” IEEE Journal of Solid-State Circuits, vol. 28, no. 6, pp. 667–670, 1993.

[48]. Vignesh NA, Kanithan S, Sravani K, Kumari CU, Swathi K, Kumareshan N, Nair PP et al., “Rapid low power voltage level shifter utilizing regulated cross coupled pull up network,” in 2021 International Conference on Computer Communication and Informatics (ICCCI). IEEE, 2021, pp. 1–9.

[49]. Basir A, Shah IA, and Yoo H, “Sphere-shaped implantable receiver coil for misalignment-resilient wireless power transfer systems for implantable devices,” IEEE Transactions on Antennas and Propagation, 2022.

[50]. Ardell JL, Nier H, Hammer M, Southerland EM, Ardell CL, Beaumont E, KenKnight BH, and Armour JA, “Defining the neural fulcrum for chronic vagus nerve stimulation: implications for integrated cardiac control,” The Journal of physiology, vol. 595, no. 22, pp. 6887–6903, 2017. [PubMed: 28862330]

[51]. Jia Y, Guler U, Lai Y-P, Gong Y, Weber A, Li W, and Ghovanloo M, “A trimodal wireless implantable neural interface system-on-chip,” IEEE transactions on biomedical circuits and systems, vol. 14, no. 6, pp. 1207–1217, 2020. [PubMed: 33180731]

[52]. Schneider UC, Bohlmann K, Vajkoczy P, and Straub H-B, “Implantation of a new vagus nerve stimulation (vns) therapy® generator, aspiresr®: considerations and recommendations during implantation and replacement surgery—comparison to a traditional system,” Acta neurochirurgica, vol. 157, no. 4, pp. 721–728, 2015. [PubMed: 25673257]

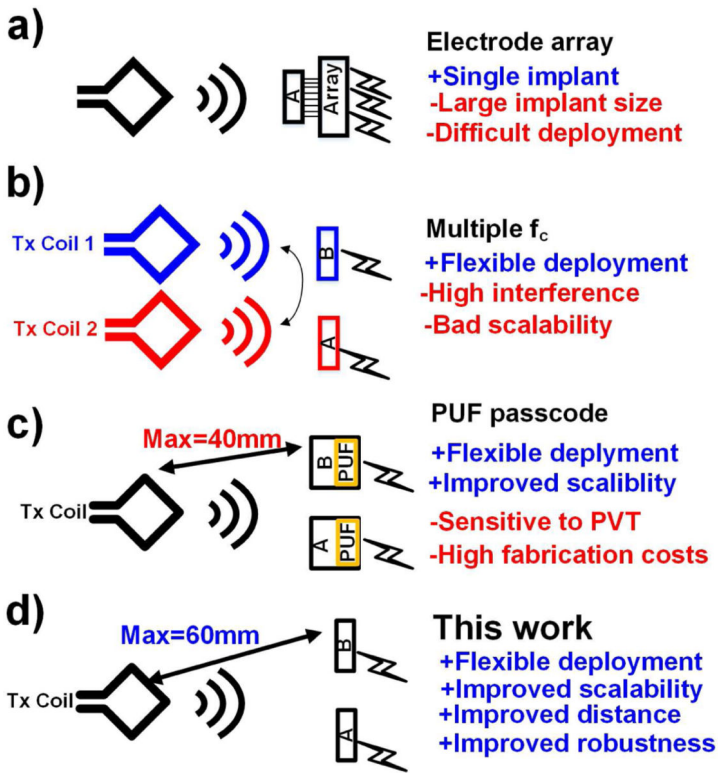

Fig. 1.

Different multisite stimulation strategies. (a) Electrode array multisite stimulation proposed in [10]. (b) The double carrier frequency for cardiac pacing presented in [3]. (c) PUF enabled IDs presented in [14]. (d) Proposed miniaturized implants based on PCB-defined passcodes.

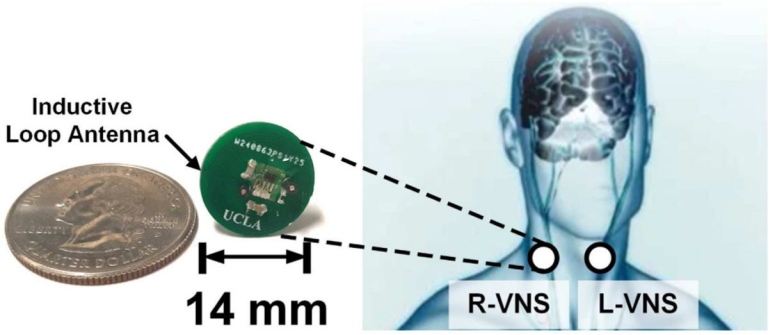

Fig. 2.
Conceptual presentation of proposed batteryless implant for bilateral VNS with a miniaturized circular coil.

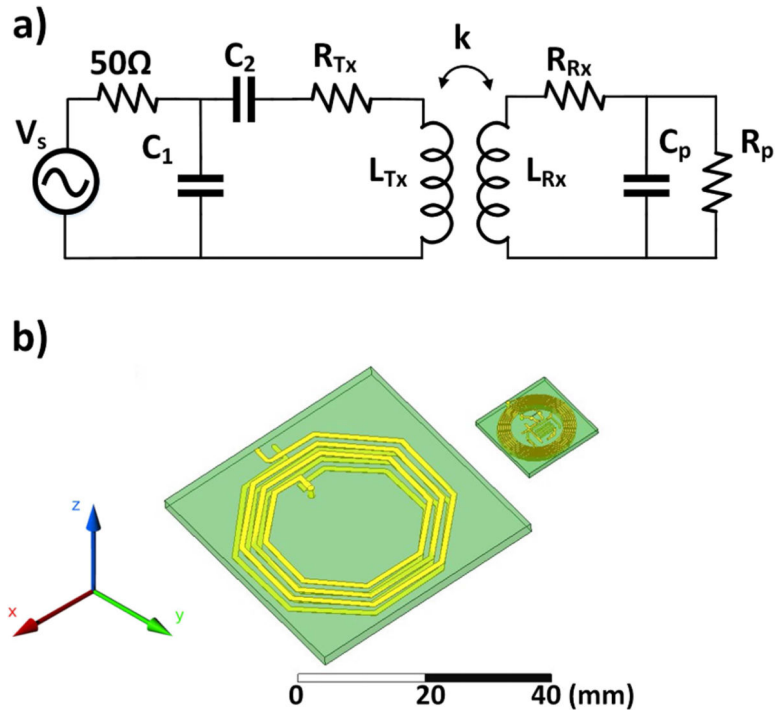

Fig. 3.

Inductive wireless power transfer link model. (a) Schematics (b) Physical size of the designed coils.

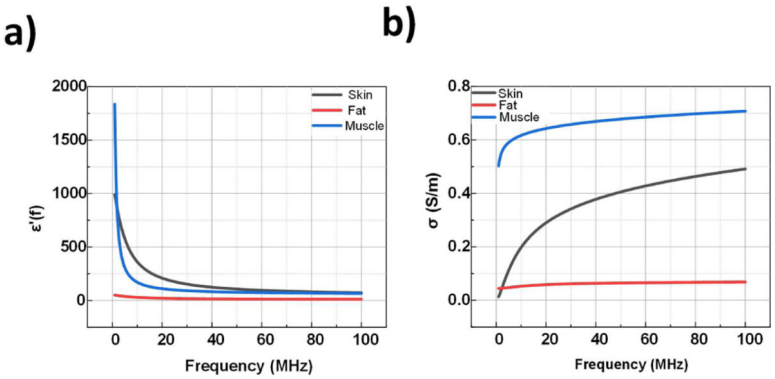

Fig. 4.

Dielectric characteristics of different biological tissues: (a) electrical permittivity (b) electrical conductivity

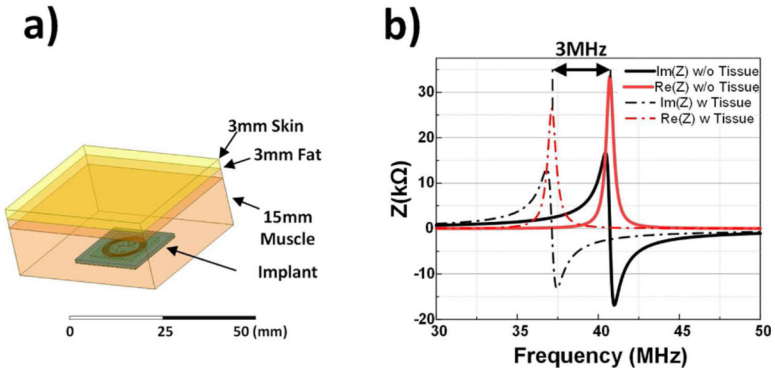

Fig. 5.

Effect of biological tissue on Rx coil resonance. (a) Modeled implant inside the neck in HFSS. (b) Drift in resonance frequency shift after adding biological tissue.

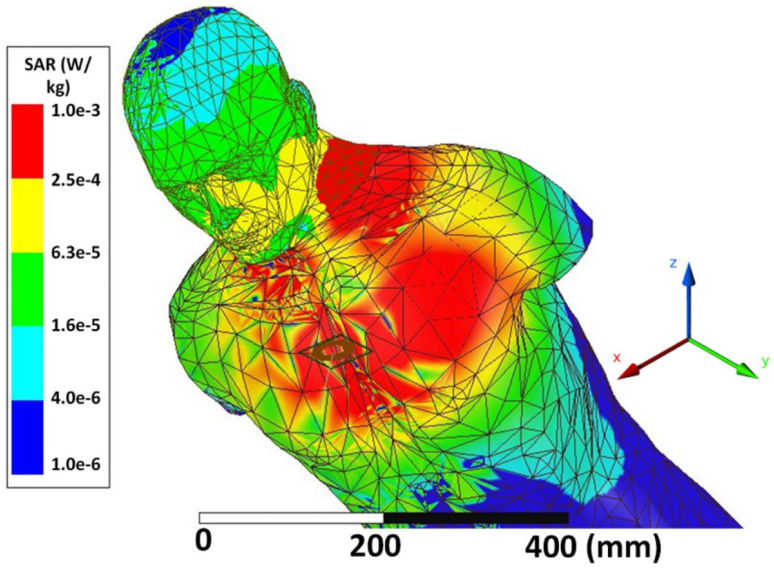

Fig. 6.
Simulated SAR over the human body in ANSYS HFSS with 1-W Tx coil

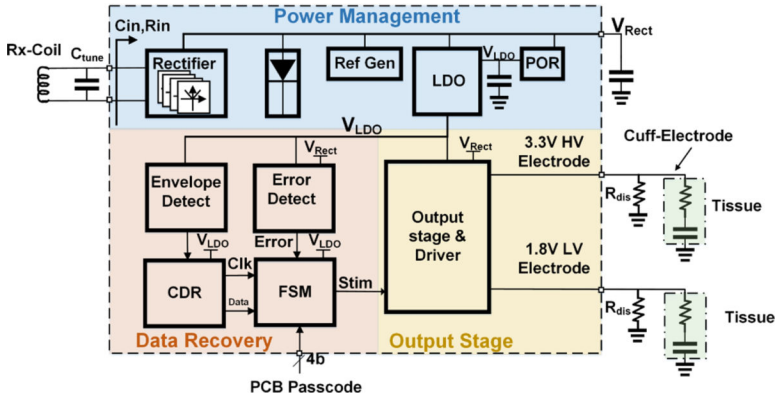

Fig. 7.
Block diagram of the proposed implant

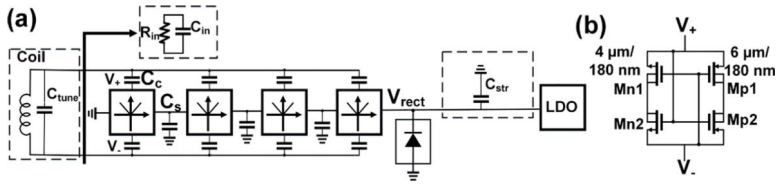

Fig. 8.

Proposed rectifier: (a) 4-stage rectifier with voltage limiter (b) One stage of CC rectifier

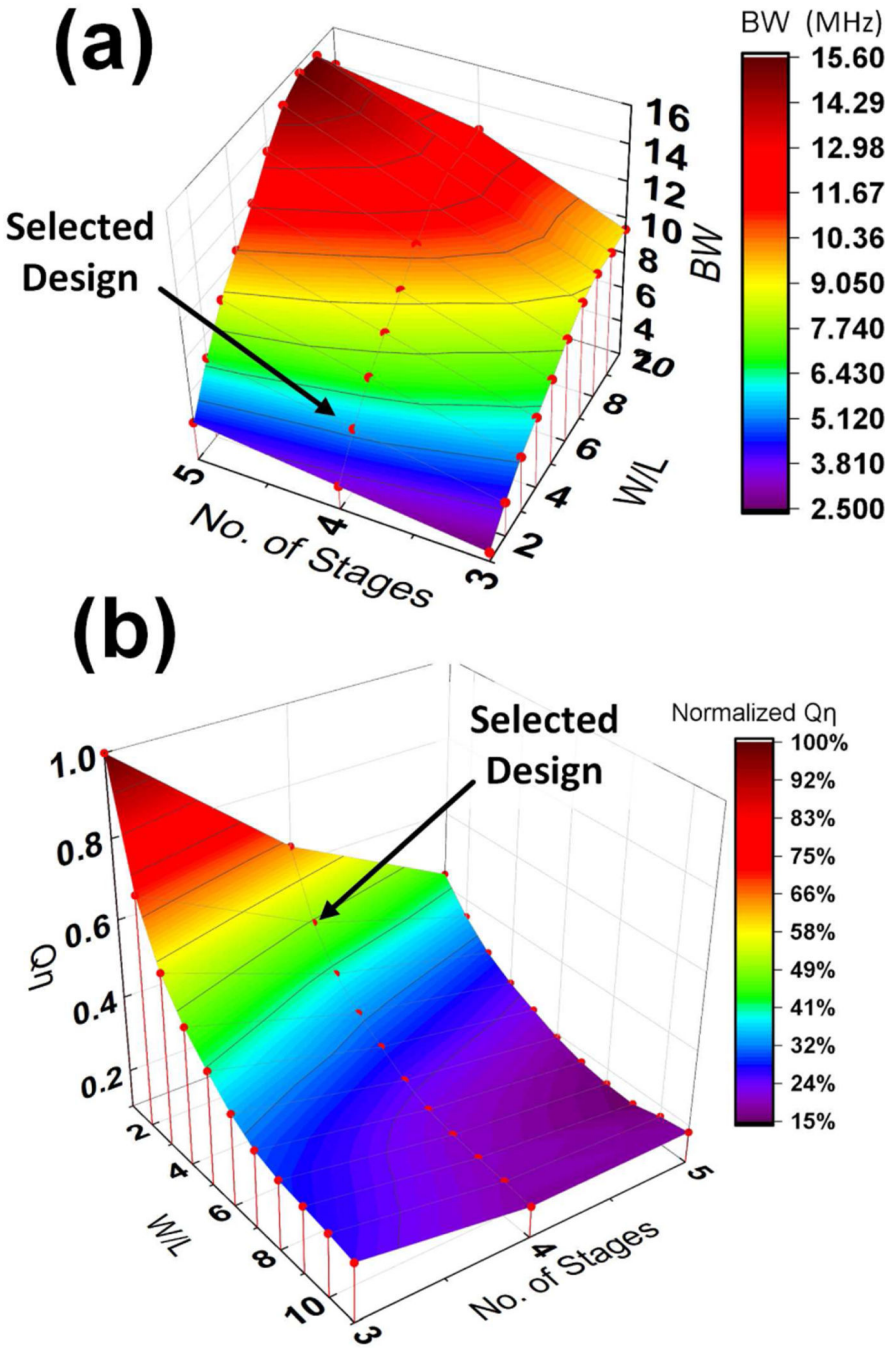

Fig. 9.

Variation of the rectifier with respect to scaling and number of stages: (a) BW (b) $Q\eta_{rect}$

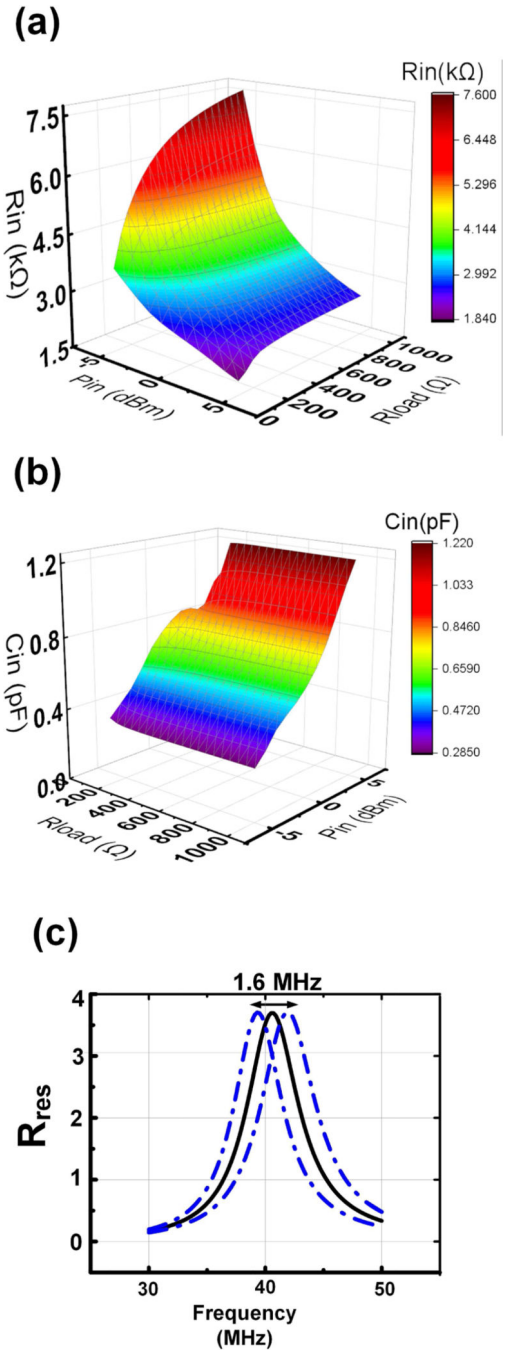

Fig. 10.

Variation of the rectifier with respect to input power and loading: (a) R_{in} (b) C_{in} (c) f_{Res}

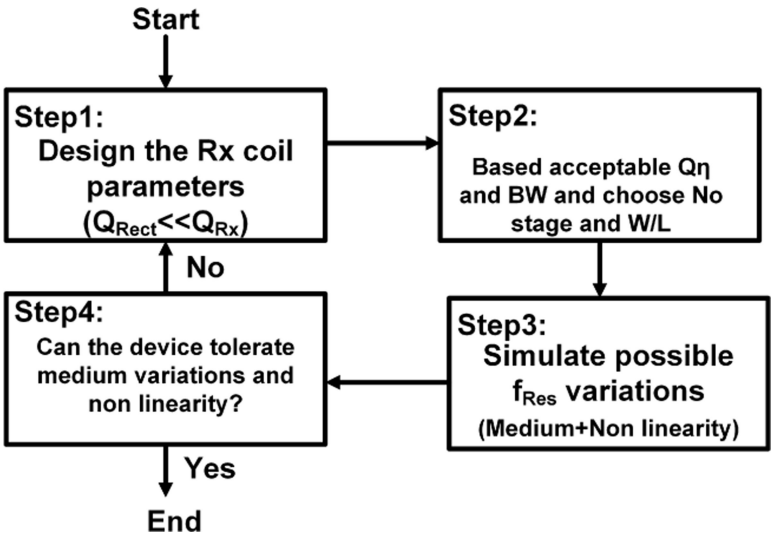

Fig. 11.
Procedure for co-designing rectifier and Rx coil for reliable operation

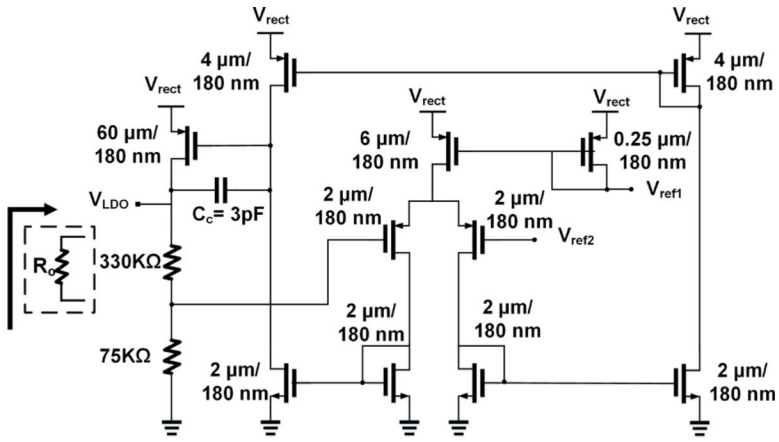

Fig. 12.
Circuit schematic of the LDO

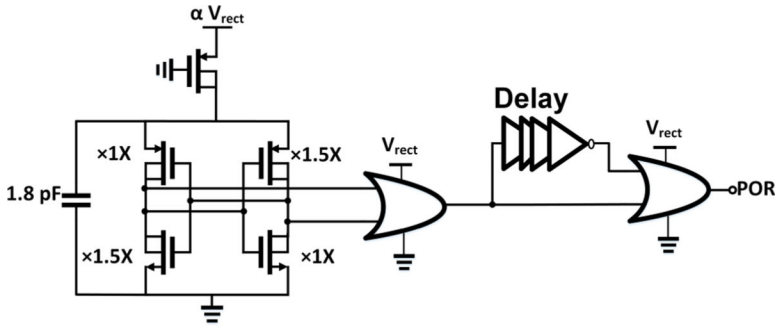

Fig. 13.
Scehmatics of POR for digital blocks

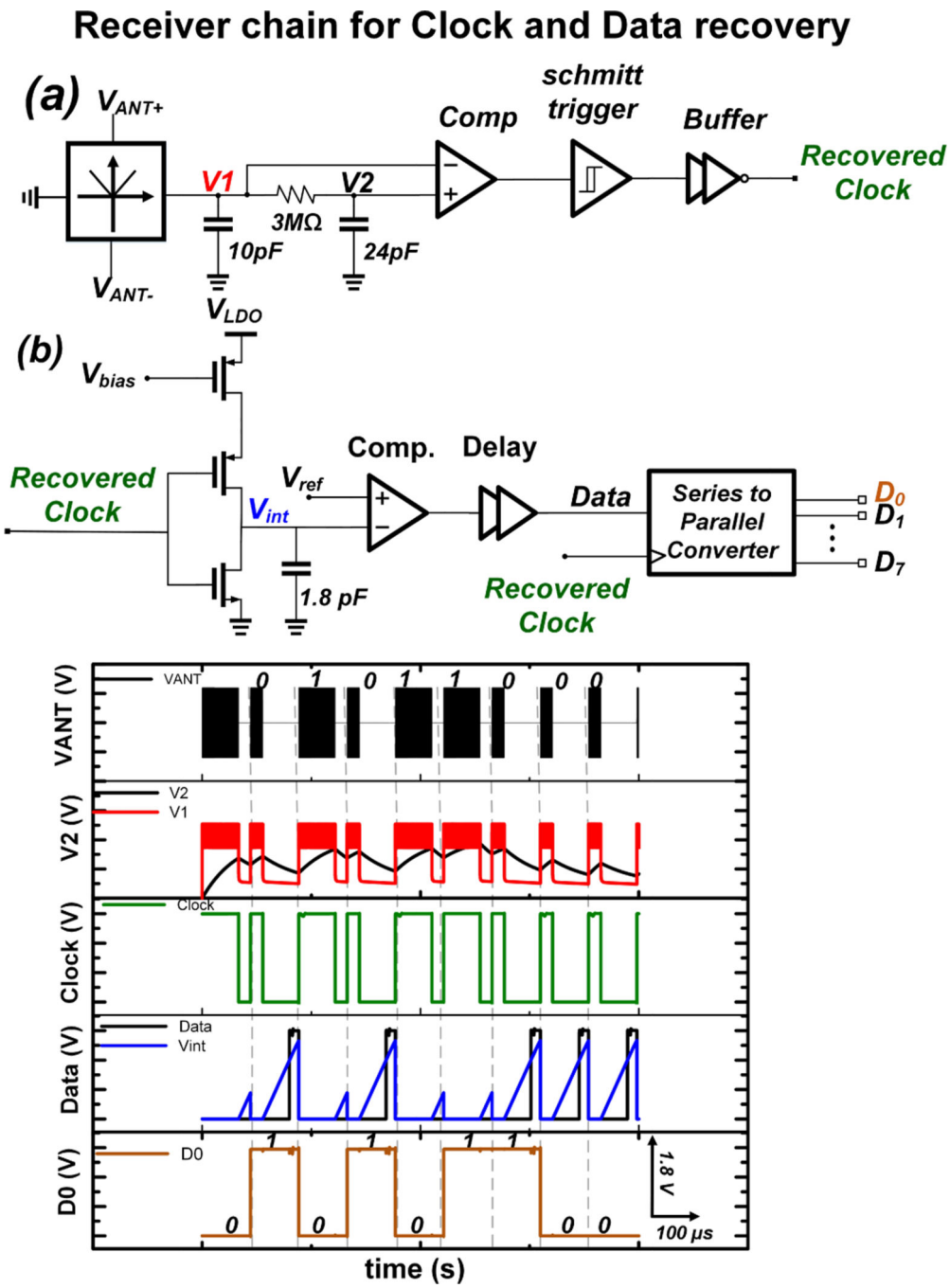

Fig. 14.

Block diagram for clock and data recovery: (a) Clock recovery chain (b) Data recovery chain

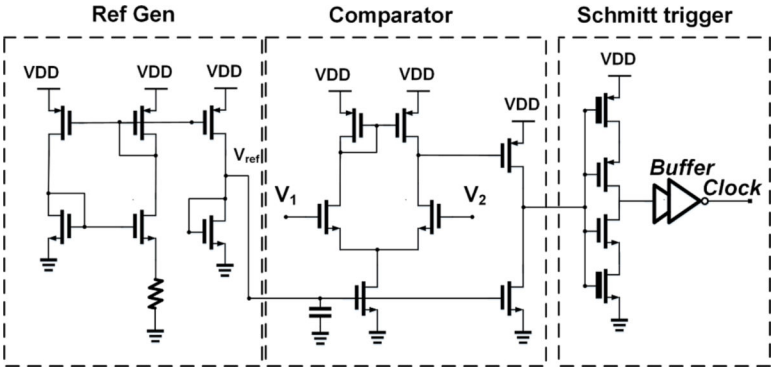

Fig. 15.
Schematic of Reference generator, comparator, and Schmitt trigger

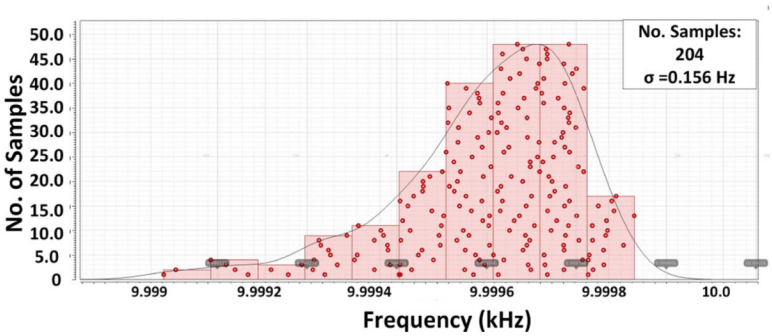

Fig. 16.
Monte Carlo simulation of the recovered clock frequency

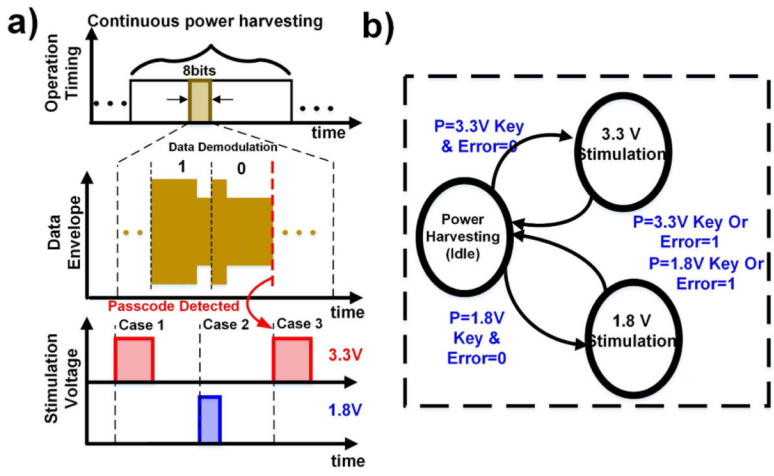

Fig. 17.
Timing diagram of the stimulator chip: (a) Conceptual presentation and (b) FSM.

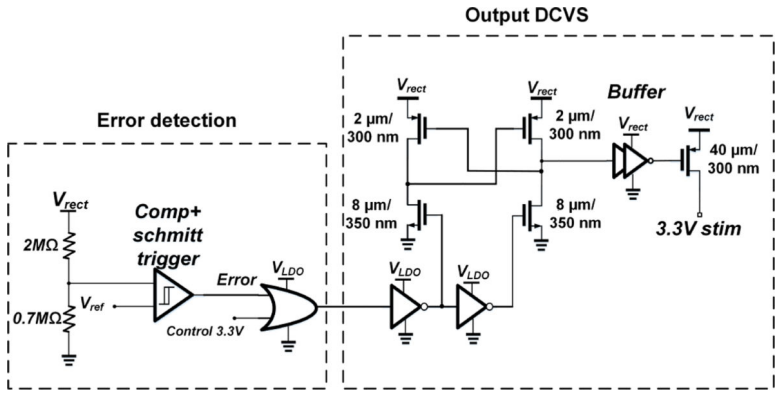

Fig. 18.

Output and control stage of the stimulator

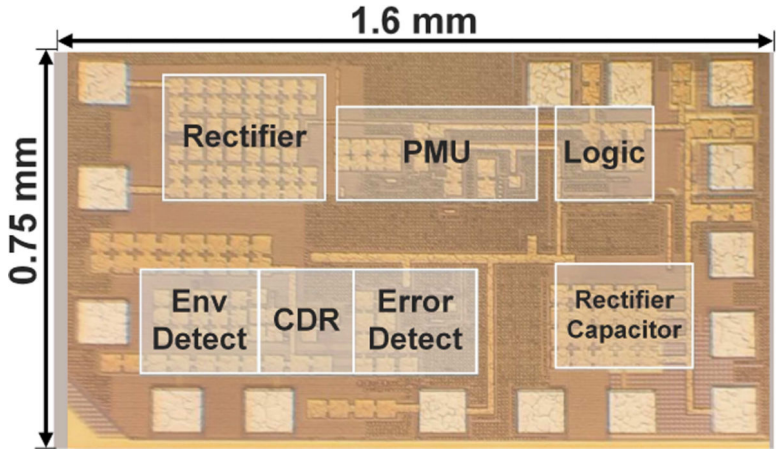

Fig. 19.
Micrograph of the Implant's SoC

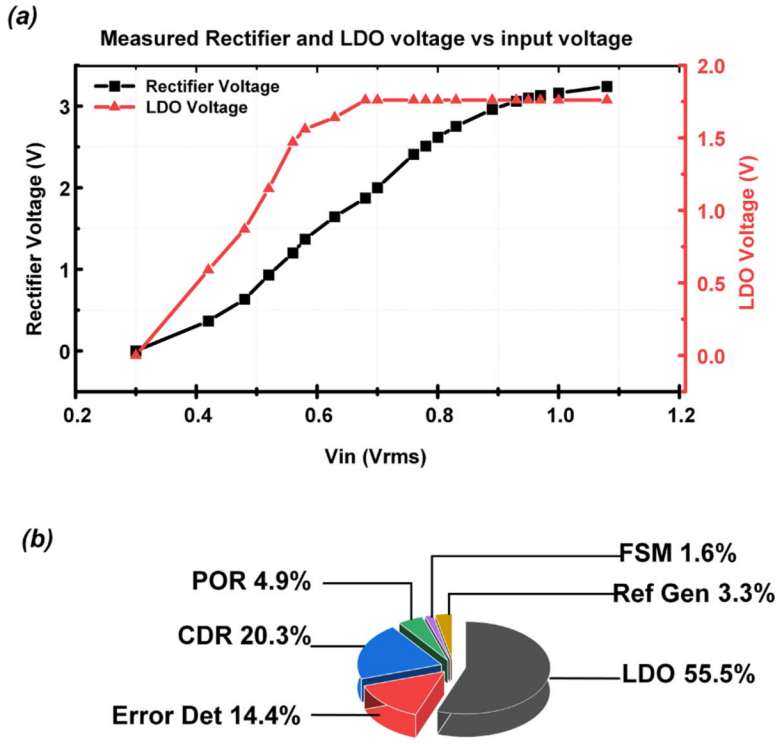

Fig. 20.

Chip power performance: (a) Measured rectified and regulated voltage and (b) Simulated power break-down

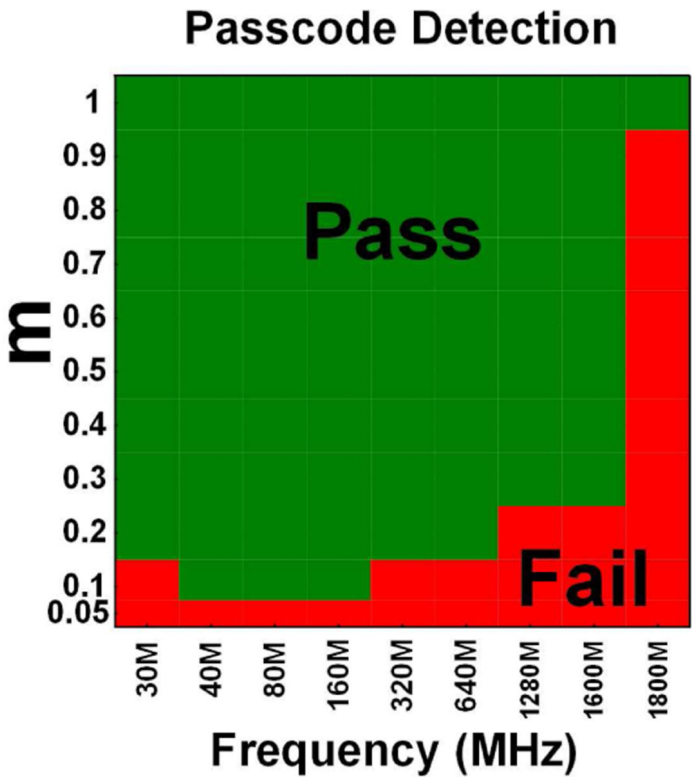

Fig. 21.
Performance of the chip at different carrier frequencies and modulation indexes.

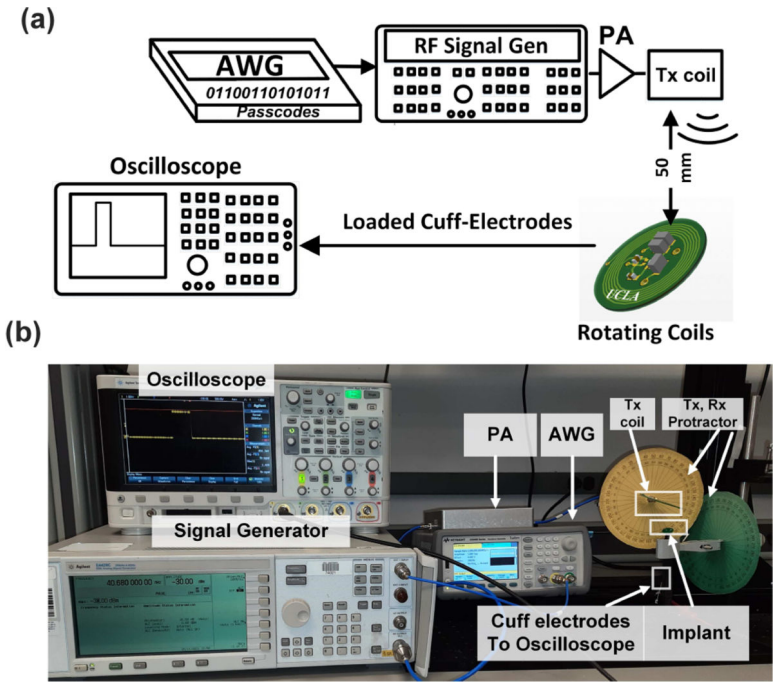

Fig. 22.

Implant validation experiment: (a) Schematic and (b) Picture of the test set up, (c) Harvested voltage Vs. distance and (d) Harvested voltage Vs.angular misalignment.

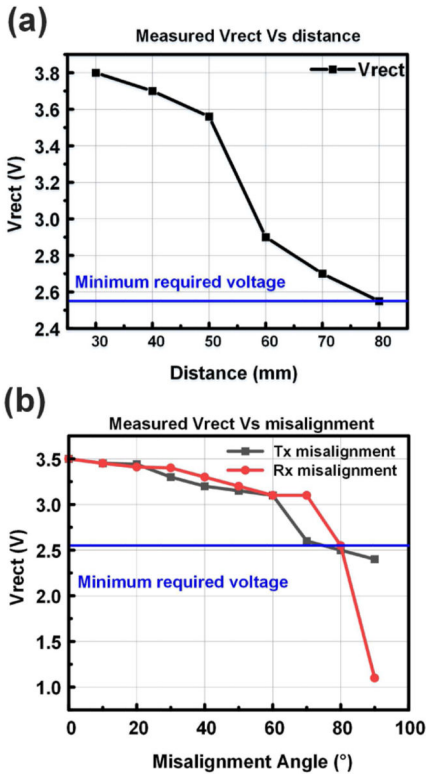

Fig. 23.

Implant validation experiment: (a) Harvested voltage Vs. distance and (b) Harvested voltage Vs.angular misalignment.

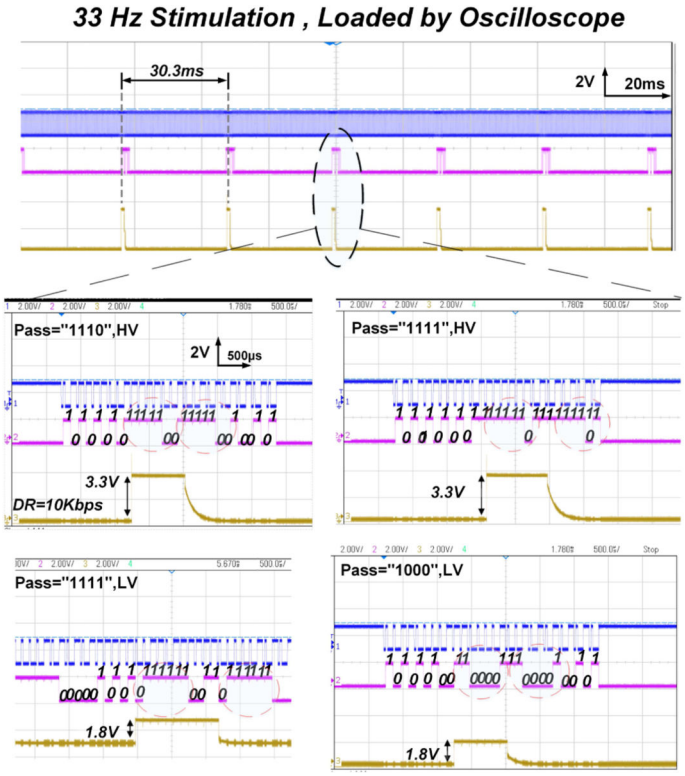

Fig. 24.
Different passcodes sent to the implant for verification

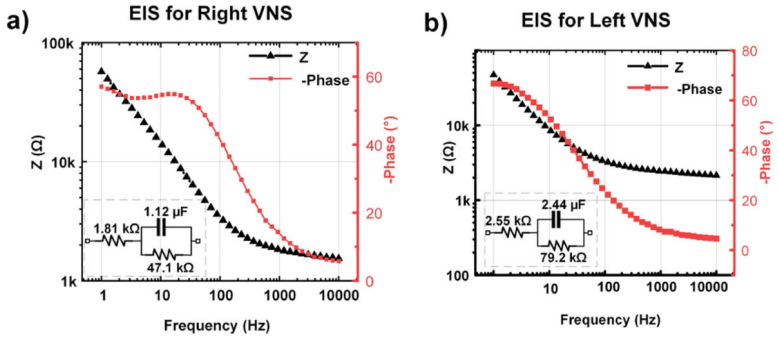

Fig. 25.
EIS and fitted circuits for a) Right VNS and b) Left VNS.

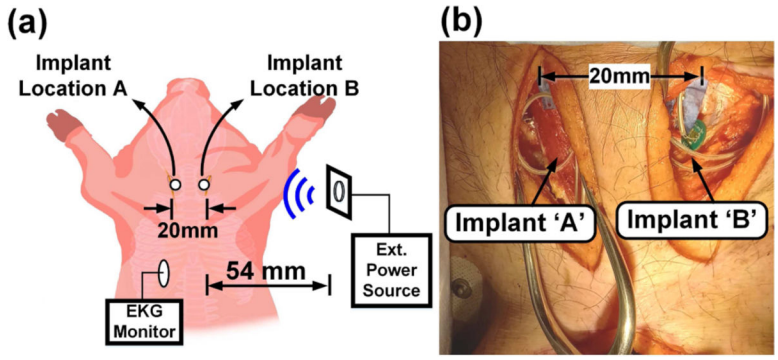

Fig. 26.
In-Vivo validation of bilateral VNS: (a) conceptual presentation of the setup (b) Implants after surgery.

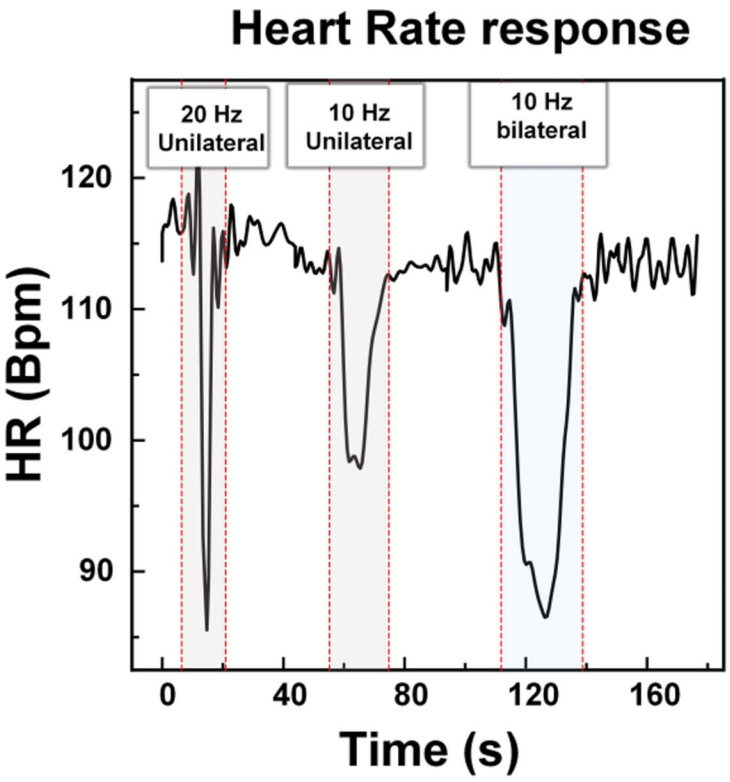

Fig. 27.
Heart response to unilateral and bilateral VNS.

TABLE I

Tx AND Rx COIL PARAMETERS

Coil parameters	Tx (Measured)	Rx (HFSS)
Dimensions	35 mm × 35 mm	14 mm diameter
No. Turns and No. Layers	6 and 2	12 and 2
Q@f_c	40.34	66.2
L@f_c	1.96 μH	1.91 μH
SRF	58.82 MHz	90.44 MHz
W and S	1.1 mm	0.18 mm

TABLE II

LDO SPECIFICATIONS

	LDO
I_Q	$7.6\mu A$
R_{on}	30 Ω
Line Reg	1.8%
Load Reg	60mV @ 1 mA

TABLE III

PERFORMANCE COMPARISON OF WIRELESSLY POWERED IMPLANTABLE DEVICES

	This work	**JSSC '22 [14]**	**Scientific Reports'21 [3]**	**TBIOCAS'20 [51]**	**Nature BME'20 [11]**	**Scientific Reports'18 [10]**	**Commercial VNS therapy device [52]**
Target application	**Neural/ Cardiac**	Neural/ Cardiac	Cardiac	Neural	Neural	Neural	Neural
Process(nm)	**180**	180	180	350	65	130	N/A
Power link	**Resonant inductive**	ME	Resonant inductive	Inductive	Ultrasonic	Inductive	Battery
Stim type	**Voltage**	Voltage	Voltage	Optical, current	Current	Current	Current
No. of channels	**2**	1	1	8	1	4	1
Pulse width	**1.2 ms, 10b**	1.2 ms, 4b	Continuous	0.64 ms, 4b	Continuous	314μs, 5b	1000μs, 3b
F_{Pulse}	**Continuous**	Continuous	Continuous	400 Hz, 4b	Continuous	13–414 Hz	Hz-30 Hz
Amplitude	**3.3 V/1.8 V**	3.5 V, 4b	3.3 V, fixed	0.77 mA, 5b	0.4 mA, 3b	60 μA −1.86 mA	3.5mA, 4.5b
Addressability	**PCB Passcode**	PUF	Different f_c	Multiplexer	N/A	Multiplexer	N/A
Chip size(mm^2)	**0.75×1.6**	1×0.8	0.85×0.45	5×3	1×1	2.4×5	N/A
SoC power(μW)	**27**	9	3.3	20700	4	35000	N/A
Implant size(mm^3)	**20.1**	6.2	10.1	N/A	1.7	2250	18657
Max Tx-Rx distance (mm)	**80(air)/ 60(PBS)**	40	60	70(estimate)	70(gel)	70	N/A
Off-chip components	**Coil+3**	ME film+1	Coil+3	Coil+ 4(estimate)	Piezo+1	coil+ 2(estimate)	Coil+9
In-Vivo test	**Pig**	Rat	Pig	Rat	Rat	Rat	FDA approved
Max Angular Misalignment	**70°@ 50mm**	50° @15mm	N/A	N/A	45° @2.2mm	N/A	N/A

IEEE Trans Microw Theory Tech. Author manuscript; available in PMC 2024 May 01.